Atmospheric Research 249 (2021) 105298

Contents lists available at ScienceDirect

Atmospheric Research

journal homepage: www.elsevier.com/locate/atmosres

On the distribution of helicity in the tropical cyclone boundary layer from dropsonde composites

Nuo Chen[a,e,f], Jie Tang[a,*], Jun A. Zhang[b,c,**], Lei-Ming Ma[d], Hui Yu[a]

[a] Shanghai Typhoon Institute, CMA, Shanghai, China
[b] NOAA/AOML Hurricane Research Division, Miami, FL, USA
[c] University of Miami, Cooperative Institute for Marine and Atmospheric Studies, Miami, FL, USA
[d] Shanghai Central Meteorological Observatory, Shanghai, China
[e] Department of Atmospheric and Oceanic Sciences, University of Wisconsin–Madison, Madison, WI, USA
[f] Cooperative Institute for Meteorological Satellite Studies, University of Wisconsin–Madison, Madison, WI, USA

ARTICLE INFO

Keywords:
Tropical cyclone
Helicity
Boundary layer
Dropsonde composite

ABSTRACT

This study analyzes GPS dropsonde data in multiple tropical cyclones from 1997 to 2017 to investigate the boundary layer structure with a focus on helicity distribution. A helicity-based method for boundary layer height is developed and evaluated by comparing it to other boundary layer height scales including the inflow layer depth, height of the maximum tangential wind speed and thermodynamic mixed layer depth. Our dropsonde composites confirmed the radial variations of these boundary layer heights seen in previous studies. The results show that the boundary layer height defined by the maximum vertical gradient of helicity is closest to the height of the maximum tangential wind speed or jet height and is located between the inflow layer depth and thermodynamic mixed layer height in all intensity groups. All three kinematic height scales generally decrease with storm intensity at a given radius. These kinematic height scales converge in the major hurricane group, while the inflow layer depth is much larger than the other two height scales in the tropical storm group. The maximum normalized helicity is located at 100–200 m altitude which is close to the height of the maximum inflow. Both front-back and downshear-upshear asymmetries are observed in the 0–1 km layer integrated helicity in the inner core region of a storm, and the helicity on the front and downshear sides is larger in all intensity groups. The results also show that the helicity magnitude is generally larger in the boundary layer of stronger storms. Application of helicity to quantify turbulent characteristics in the boundary layer is discussed.

1. Introduction

Tropical cyclone (TC) intensity is influenced not only by environmental conditions but also by inner-core physical processes. Previous theoretical studies have pointed out the important role of boundary-layer turbulent processes in TC intensity and potential maximum intensity (e.g., Emanuel, 1986; Wang and Wu, 2004; Riemer et al., 2010; Smith et al., 2009, 2017; Wang, 2012; Kieu et al., 2014; Zhang and Marks, 2015; Montgomery and Smith, 2014; Chen et al., 2019).

Previous numerical studies have also demonstrated the critical role of boundary-layer physics in simulations of hurricane intensity and structure (Braun and Tao, 2000; Foster, 2009; Nolan et al., 2009a; Nolan et al., 2009; Smith and Thomsen, 2010; Kepert, 2012; Zhu et al., 2013; Ming and Zhang, 2016; Bu et al., 2017; Zhang et al., 2017a; Zhang and Rogers, 2019). Furthermore, accurate representation of sub-grid-scale processes such as those in the TC boundary layer (TCBL) is essential for operational TC forecasts. Recent upgrades of turbulence parameterizations in the Hurricane Weather and Research Forecast model (HWRF) have significantly improved TC intensity forecasts, emphasizing the usefulness of observational data for physics evaluation and tuning (Tallaprgada et al., 2014; Zhang et al., 2015; Zhang et al., 2018; Tang et al., 2018; Zhu et al., 2019)

Observational studies have documented both the axisymmetric and asymmetric TCBL structure by compositing a good number of dropsonde data (e.g. Zhang et al., 2011a Z11 hereafter, Ming et al., 2015; Ren et al., 2019, 2020). Z11 presented the axisymmetric TCBL structure. Ahern et al. (2019) investigated axisymmetric structural differences in the TCBL among intensifying, steady-state and weakening TCs using dropsonde composites, and found that non-intensifying TCs have larger tangential winds and stronger radial inflow but smaller entropy

* Corresponding author at: Shanghai Typhoon Institute, CMA, Shanghai, China.
** Corresponding author at: NOAA/AOML Hurricane Research Division, Miami, FL, USA.
E-mail addresses: tangj@typhoon.org.cn (J. Tang), jun.zhang@noaa.gov (J.A. Zhang).

https://doi.org/10.1016/j.atmosres.2020.105298
Received 12 May 2020; Received in revised form 28 September 2020; Accepted 30 September 2020
Available online 01 October 2020

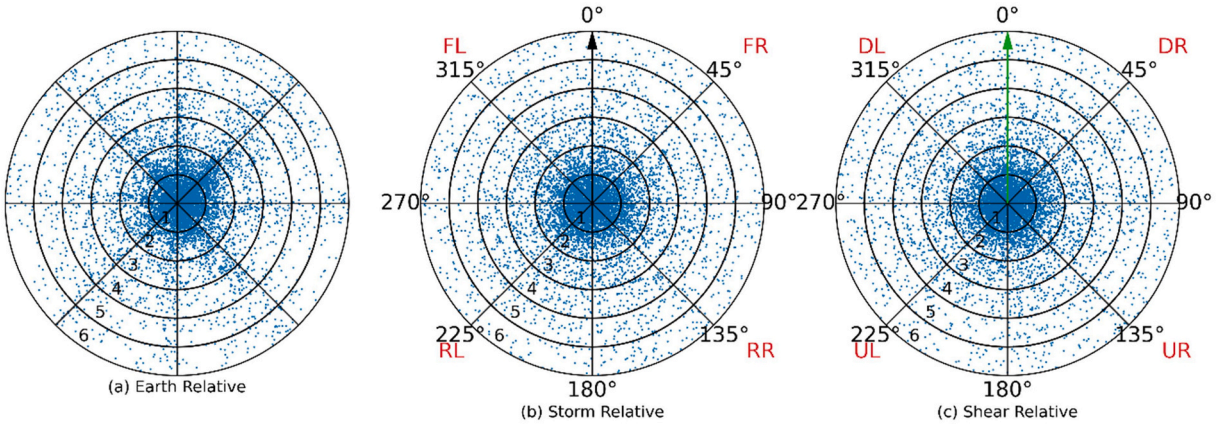

Fig. 1. Horizontal distribution of dropsonde data in (a) earth-relative, (b) storm-relative, and (c) shear-relative frameworks. The radius is normalized by the radius of maximum wind speed. In (b), the black arrow represents the storm motion direction. FL, FR, RL and RR represents front-left, front-right, rear-left and rear-right quadrant, respectively. In (c), the green arrow represents the shear direction. DL, DR, UL and UR represents downshear-left, downsheare-right, upshear-left and upshear-right quadrant, respectively.

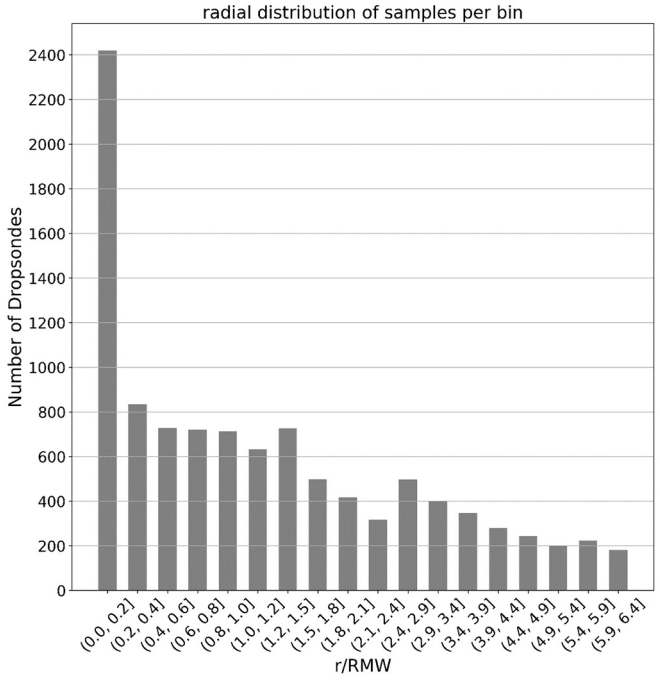

Fig. 2. Radial distribution of sample size in each radial bin used for the composite analysis. The radial distance (r) is normalized by the radius of maximum wind speed (RMW).

outside the radius of maximum wind speed (RMW) than intensifying TCs. Nguyen et al. (2019) studied the impacts of downdrafts on asymmetric TCBL thermal structure and TC intensity change through dropsonde composite analyses. They found that larger conditional instability occurred on the downshear side and greater surface enthalpy fluxes were located on the upshear side in more rapidly intensifying TCs. Zhang et al. (2020) documented the diurnal variation of the TCBL structure using dropsonde composites. Furthermore, previous studies have analyzed dropsonde data to investigate the BL structure of an individual TC during various stages of intensity change (e.g., Kepert, 2006a, 2006b; Barnes, 2008; Bell and Montgomery, 2008; Molinari et al., 2013; Montgomery et al., 2014; Rogers et al., 2015, 2016; Zawislak et al., 2016; Zhang et al., 2017b; Wadler et al., 2018).

When vertical profiles of turbulent fluxes are measured, the boundary layer height is usually taken as the height where the magnitude of the turbulent flux is ~5% of that in the surface layer. Note that the surface layer height is close to 10% of the boundary layer height (Stull, 1988). Without high-frequency observational data, the boundary layer height can be estimated using mean boundary layer quantities. The height of the sharpest temperature gradient is generally used to define the boundary layer height in an unstable condition, while the vertical gradient of virtual potential temperature with a specific threshold is used for stable or neutral boundary layers (Fetzer et al., 2004; Medeiros et al., 2005). Zhang and Drennan (2012) showed that turbulent fluxes are close to zero.

near the top of the inflow layer of the TC outer region (100–150 km radii) based on in-situ aircraft observations. However, Guimond et al. (2018) showed that both the turbulent kinetic energy (TKE) and momentum flux are not negligible near the top of the inflow layer of both primary and secondary eyewalls of Hurricane Rita (2016) using radar observations. Lorsolo et al. (2010) observed large values of TKE in the hurricane eyewall region up to 13 km altitude using Doppler radar data. Thus, it is still uncertain where is the top of the boundary layer in the TC eyewall or rainband region from turbulent flux or TKE point of view. Numerical and theoretical studies also discussed the difficulty of defining the TCBL height in the eyewall region (Smith and Montgomery, 2010; Zhu et al., 2019), given that few flux observations exist below 450 m altitude in intense hurricanes (Marks et al., 2008; Zhang et al., 2011b; Zhao et al., 2020; Cione, 2020).

Three height scales were evaluated by Z11 for the TCBL using dropsonde composites, including the inflow layer depth (h_{infl}), the height of the maximum tangential wind speed (h_{vmax}), and thermodynamic mixed layer height (Z_i). Z_i is depicted by the height where the thermal stability ($d\,\theta_v/dz$) is equal to 3 K km^{-1} following Zeng et al. (2004), where v is θ_v the virtual potential temperature. The height of 10% of maximum inflow is taken as h_{infl}. Z11 showed that these three height scales generally increase with radius, especially outside the RMW in hurricanes over the Atlantic basin. This structure was confirmed in TCs over other ocean basins and those with different strengths (Ming et al., 2015; Ren et al., 2020). Similar radial variation of these height scales was seen in both shear-relative and motion-relative TC dropsonde composites (Zhang et al., 2013; Ren et al., 2019).

Helicity is an important parameter for studying flow characteristics in fluid dynamics (Krainchnan, 1967; Moffatt, 1983; Krause and Rädler, 1980; Moffat and Tsinober, 1992; Frisch, 1995). Helicity has been used to quantify flow characteristics of mid-latitude weather phenomena, such as frontal systems (e.g. Tan and Wu 1994; Pichler and Schaffhauser, 1998) and tornadic supercells (e.g. Weisman and Rotunno, 2000). Hide (1989, 1992) and Chkhetiani (2001) found that helicity is highly correlated to the Ekman spiral profiles in the atmospheric boundary layer in non-TC conditions. As turbulent mixing in the

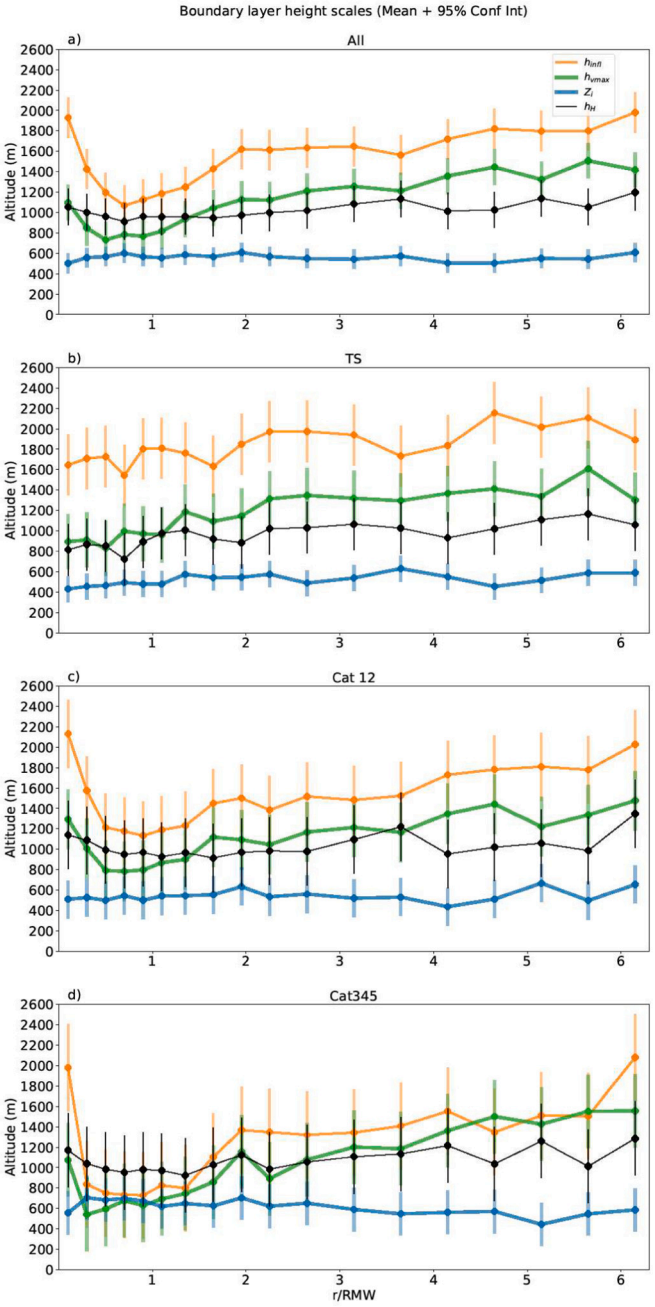

Fig. 3. Plots of four boundary layer height scales as a function of radius normalized by the radius of maximum wind speed for a) All data composite, b) tropical storm composite, c) category 1–2 hurricane composite, and d) category 3–5 hurricane composite. In each panel, h_{inf} is the inflow layer depth (orange line), h_{vmax} is the height of the maximum tangential wind speed (green line), Z_i is the mixed layer depth (blue line), and h_H is the helicity-based boundary layer height (black line). (For interpretation of the references to color in this figure legend, the reader is referred to the web version of this article.)

boundary layer is reflected by the magnitude of vertical wind shear, Levy et al. (1990) used helicity to characterize turbulent flow. Helicity was also used to quantify the strength of fine-scale vortices or coherent structures in the boundary layer in the past (Moffatt, 1983; Moffat and Tsinober, 1992; Brown, 1970; Etling, 1985).

Bogner et al. (2000) presented the distribution of helicity in TCs using dropsonde data. Similarly, Molinari and Vollaro (2008) found large helicity values in the TCBL of Hurricane Bonnie (1998). Molinari and Vollaro (2010) also documented large values of helicity in the TCBL in numerical simulations. Onderlinde and Nolan (2014) pointed out that a positive helicity environment is favorable for TC intensification. Ma and Bao (2016, MB16 hereafter) proposed a method to parameterize the boundary layer height using helicity in the Weather and Research Forecast (WRF) model and found that their method improved the intensity simulation of Typhoon Morakot (2009).

In the present study, we evaluate the helicity-based method for defining the boundary layer height using dropsonde data and compare it to other scaling methods. As a follow-up of previous TCBL studies, we further investigate the TCBL structure using dropsonde data with a focus on the distribution of helicity in a climatology sense. Section 2 describes definition of helicity. Section 3 presents the data and analysis method. Section 4 presents data analysis results including the boundary layer heights and helicity distributions. This is followed by discussions and conclusions.

2. Helicity

Helicity ($\mathscr{H}$) is a measure of the degree to which the direction of fluid motion is aligned with that of the vorticity (e.g. Davies-Jones, 1984; Markowski and Richardson, 2010), and the horizontal component of this scalar is related to stream-wise vorticity. $\mathscr{H}$ is defined as the dot product of velocity (v) and vorticity ($\omega = \nabla \times \vec{v}$) vectors in the form of:

$$H = \vec{v} \cdot \nabla \times \vec{v} = (u\vec{i} + v\vec{j} + w\vec{k}) \cdot \left[\left(\frac{\partial w}{\partial y} - \frac{\partial v}{\partial z} \right)\vec{i} + \left(\frac{\partial u}{\partial z} - \frac{\partial w}{\partial x} \right)\vec{j} + \left(\frac{\partial v}{\partial x} - \frac{\partial u}{\partial y} \right)\vec{k} \right] = u\left(\frac{\partial w}{\partial y} - \frac{\partial v}{\partial z} \right) + v\left(\frac{\partial u}{\partial z} - \frac{\partial w}{\partial x} \right) + w\left(\frac{\partial v}{\partial x} - \frac{\partial u}{\partial y} \right) \quad (1)$$

For helicity calculation using vertical profiles of wind velocities measured a dropsonde, Eq. (1) is simplified to $H = \frac{du}{dz} \cdot v - \frac{dv}{dz} \cdot u$, because the component, $u\frac{\partial w}{\partial y} - v\frac{\partial w}{\partial x} + w\left(\frac{\partial v}{\partial x} - \frac{\partial u}{\partial y}\right)$, can not be obtained from the dropsonde profiles. At a given vertical level (e.g., i_{th} level), the helicity is computed as:

$$H_i = v_i \frac{u_i - u_{i-1}}{z_i - z_{i-1}} - u_i \frac{v_i - v_{i-1}}{z_i - z_{i-1}} \quad (2)$$

where u and v are radial and tangential wind velocity, respectively. It is important to note that the helicity is a scalar, so it only has a positive or negative value. The column integrated helicity over the lowest 1 km layer is computed as:

$$<H> = \sum_{i=sfc}^{1km} H_i dz = \sum_{i=sfc}^{1km} \left(v_i \frac{u_i - u_{i-1}}{z_i - z_{i-1}} - u_i \frac{v_i - v_{i-1}}{z_i - z_{i-1}} \right) dz \quad (3)$$

MB16 defined the boundary layer height using the maximum of the absolute value of the first-order vertical derivative of the helicity at each model column, in the forms of:

$$h_{\mathscr{H}} = \max\left(\left| \frac{\partial \mathscr{H}_i}{\partial z_i} \right| \right) \quad (4)$$

$$h_{\mathscr{H}} = \max\left(\left| \frac{\partial \mathscr{H}_i}{\partial z_i} \right| \right) \cap \min\left(\left| \frac{\partial^2 \mathscr{H}_i}{\partial {z_i}^2} \right| \right) \quad (5)$$

here, we use the same method as in MB16 to calculate the TCBL height using the dropsonde data that will be described in the next section.

3. Data description and analysis method

A total of about 14,000 global positioning systems (GPS) dropsondes were collected by National Oceanic and Atmospheric Administration (NOAA) and Air force aircraft during a time span from 1997 to 2017. Raw dropsonde data in the Airborne Vertical Profiling System (AVAPS)

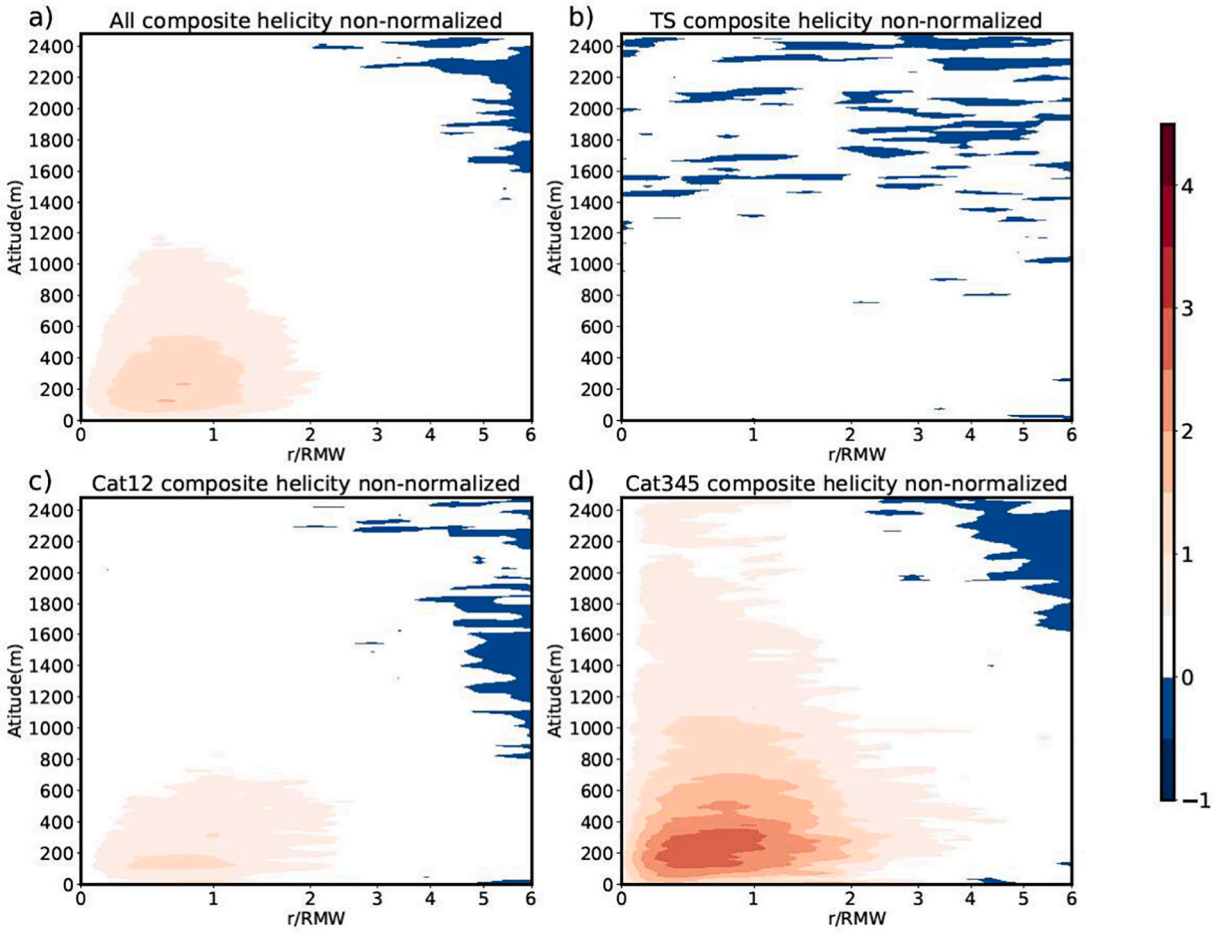

Fig. 4. Plots of azimuthally averaged helicity as a function of the normalized radius and height for a) All data, b) tropical-storm group, c) category 1–2 hurricane group, and d) category 3–5 hurricane group.

(https://www.aoml.noaa.gov/hrd/data_sub/hurr.html) include GPS longitude, latitude, pressure, horizontal wind speed and direction, vertical wind speed, relative humidity, temperature, and derived geopotential altitude. Typical error for wind speed in the AVAPS data is 0.3–2.0 m/s, 0.15 K for temperature, and 10–15% for humidity. The vertical sampling rate is 2 Hz (about 6–7 m) (e.g. Hock and Franklin, 1999). Raw data is quality controlled and data from 11,432 dropsondes are retained and analyzed in this study.

These dropsondes were collected by aircraft reconnaissance and research missions in 221 TCs. The earth-relative distribution of the dropsondes are shown in Fig. 1a where the radius is normalized by the RMW ($r^* = r/RMW$). We also rotate the data location in a storm-relative (Fig. 1b) and shear-relative (Fig. 1c) framework. Four storm-relative quadrants are labeled in Fig. 1b: front right (FR), front left (FL), rear right (RR), and rear left (RL). Similarly, four shear-relative quadrants are labeled in Fig. 1c: downshear-right (DR), downshear-left (DL), upshear-right (UR), and upshear-left (UL). It is evident from Fig. 1 that the dropsonde data are nearly evenly distributed at all azimuths at a given radius. The sampling size is the largest close to the storm center ($r^* < 0.2$), and it is the second largest at $0.2 < r^* < 1.5$ (Fig. 2). The sample size generally decreases with radius for $r^* > 1.5$. Here, we estimated the RMW using surface winds measured by the Stepped Frequency Microwave Radiometer (SFMR) following Zhang et al. (2013) for NOAA P3 and Air Force C-130 flights. For G-IV flights, we used the RMW from the extended Best track (Demuth et al., 2006).

When we composite the dropsonde data following Z11, we use a vertical bin of 10-m, an azimuthal bin of 22.5°, and a radial bin of 0.2 r^* for $r^* < 1.2$, 0.3 r^* for $r^* < 2.4$ and 0.5 r^* for $r^* > 2.4$ based on the sample distribution. In the composite analysis, we only used dropsonde data that have no data gaps within a 50 m layer. Each observation at a given altitude is considered as a random sample in the composite analysis. Three intensity groups are considered in the composite analyses: Tropical Storm (TS), Cat1-2 Hurricane (Cat12), and Cat3-5 Hurricane (Cat345). We also compare the results from these three groups to that using all data (ALL).

Tangential and radial wind velocities are computed from the horizontal wind speed and direction along with the storm center that is interpolated to the dropsonde time using the 2-min storm track from the Hurricane Research Division. This storm track was created using a combination of aircraft center fixes and 6-h interval Best Track Data following Willoughby and Chelmow (1982). Note that there is no 2-min storm track available for a total of 1424 dropsondes and their associated storm locations are computed using the Best track data.

The helicity profile is calculated using the wind velocities from an individual dropsonde. To get the helicity-based boundary layer height, we first calculate the first derivative of the composited helicity profile, then fit the derivative profile with a 5th order polynomial equation. Note that the result is the same when a higher order polynomial fitting was used. The boundary layer height is then determined using Eqs. (4) and (5). Since the magnitude of turbulent flux typically increases from the top of the boundary layer to surface (Zhang and Drennan, 2012), we search for the maximum gradient starting from the highest level of observations. All boundary layer height scales are presented in two ways: 1) the height scales are computed for an individual dropsonde and then radially averaged; 2) The height scales are computed using the composited variables. The 0–1 km layer integrated helicity is presented

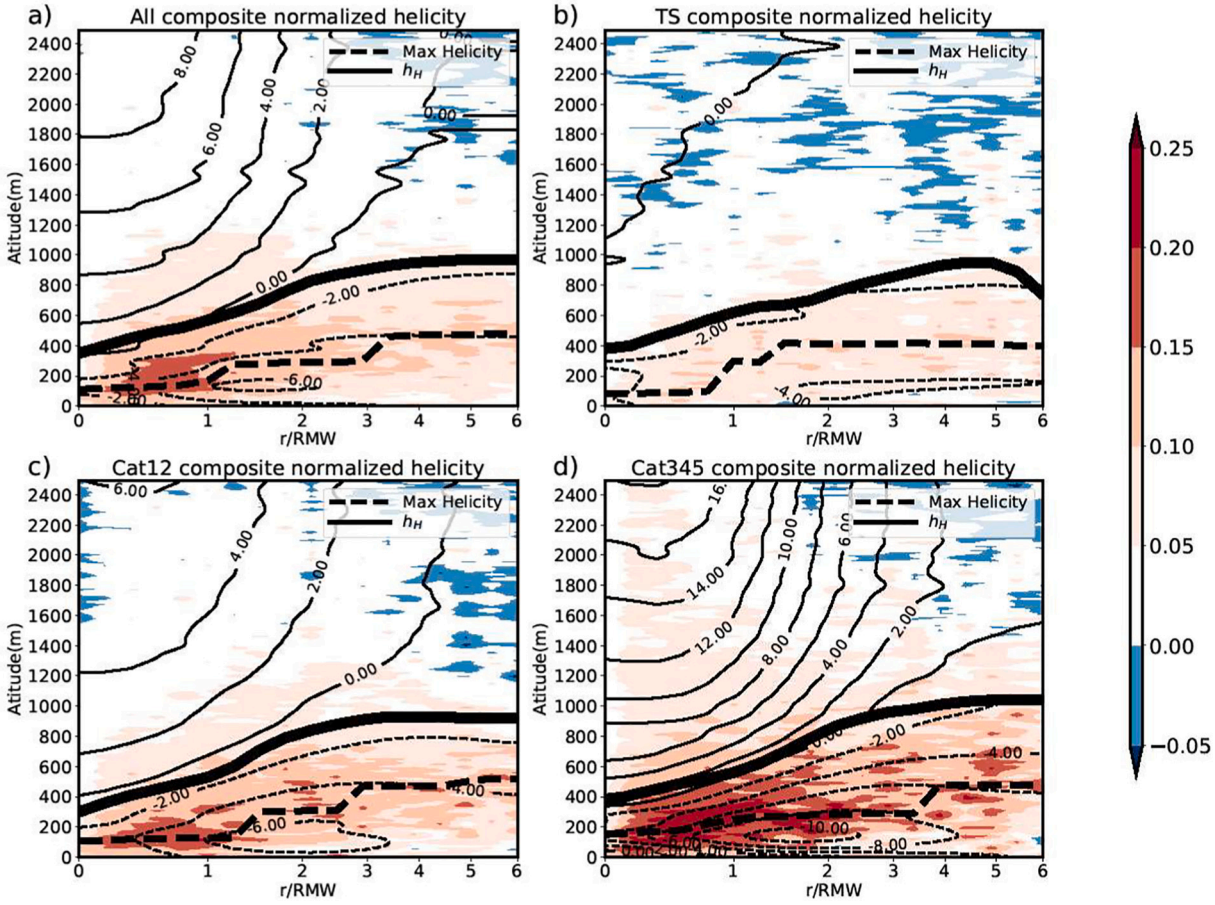

Fig. 5. Plots of azimuthally averaged normalized helicity (shading) as a function of altitude and the normalized radius for a) All data, b) tropical-storm group, c) category 1–2 hurricane group, and d) category 3–5 hurricane group. Black contours show the radial wind velocity (in m/s) with thin solid lines representing the outflow and thin dashed lines representing inflow. The height of maximum normalized helicity is shown by the thick dashed black line. The helicity-based boundary layer height is depicted by the thick black line.

in both storm-relative and shear-relative frameworks. The 850–200 hPa environmental shear data is from the ECMWF ERA5 product (Simmons and Coauthors, 2020).

4. Results

We first compare four types of the boundary layer heights (i.e., h_{vmax}, h_{infl}, Z_i, and h_H) and their radial variations among the intensity groups (Fig. 3). The height scales in Fig. 3 are the averages of those estimated using individual dropsondes. We will show later the radial variations of these height sales in the composite for each intensity group. All intensity groups captured the general increase trend of the kinematic boundary layer heights with radius as seen in the result of all data. The radial variation of Z_i is the smallest among all TCBL height scales. The results in terms of h_{vmax}, h_{infl}, Z_i confirmed those of Z11 and Ren et al. (2020). h_{vmax} and h_{infl} decrease with the increasing TC intensity at a given radius. h_{infl} is the largest while Z_i is the smallest among these height scales, indicating a large difference between the thermodynamic and kinematic TCBL heights and this difference is statistically significant. h_H is found to be closest to h_{vmax} in all intensity groups with no statistically significant difference. This result indicates that the boundary layer height based on the helicity method is similar to h_{vmax} that represents the height of boundary layer jet. Interestingly, all three kinematic TCBL height scales for the Cat345 group are close to each other, while the difference between hvmax and h_{infl} are the largest for the TS group.

Fig. 4 compares the azimuthally averaged helicity composite for all data and those for the three intensity groups. Composite of all samples shows a helicity maximum of 2 m/s^2 located inside the RMW at ~100 m altitude (Fig. 4a). Negative helicity with a relatively small magnitude is located at $r^* > 2$ above 1200 m altitude and near the surface. This negative helicity may be due to the wind decay above the boundary layer. In the TS composite, the helicity is all negative with a magnitude of ~1 m/s^2 above 1200 m altitude (Fig. 4b). Helicity composites of Cat12 and Cat345 groups show similar structure as that of all data, except that the magnitude of the helicity is different, especially inside $r^* = 3$. The maximum helicity in the Cat345 composite nearly triples that in the Cat12 composite. The area of strong helicity greater than 1 m/s^2 in the Cat345 composite is at the region of $0.5 < r^* < 2$ and extends to 1000 m altitude. The area coverage of helicity with large values (> 0.5 m/s^2) increases with storm intensity. This result suggests stronger turbulent mixing occurs in the TCBL of more intense TCs.

To further study the distribution of helicity in the TCBL in a climatological sense and reduce the effect of storm intensity or wind speed on the helicity distribution, we normalize the helicity by the maximum value of a dropsonde profile before compositing the data for each intensity group. Figs. 5 and 6 show the composites of normalized helicity as a function of normalized radius and height, with composites of radial wind and tangential wind, respectively. The thick solid black line shows the maximum vertical gradient of helicity, while the thick dashed black lines shows the height of maximum helicity in each panel of Figs. 5 and 6.

The normalized helicity composites have a broader area of positive values than the non-normalized helicity composites. All intensity

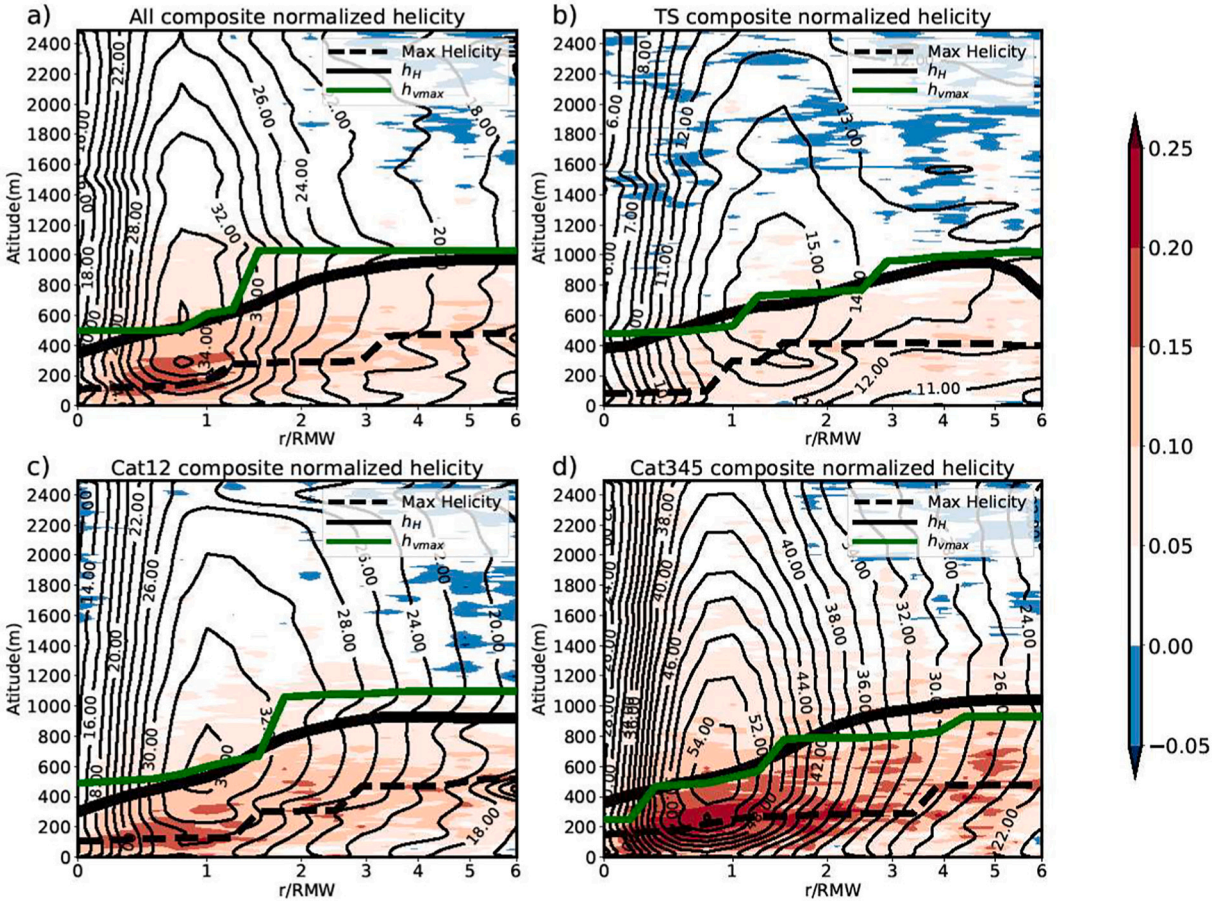

Fig. 6. Plots of azimuthally averaged normalized helicity (shading) as a function of altitude and the normalized radius for a) All data, b) tropical-storm group, c) category 1–2 hurricane group, and d) category 3–5 hurricane group. Black contours show the tangential wind velocity (in m/s). The height of maximum normalized helicity is shown by the thick dashed black line. The helicity-based boundary layer height is depicted by the thick black line. The height of the maximum tangential wind speed is depicted by the thick green line.

groups show a similar vertical variation of the helicity except that the magnitudes of helicity at each vertical level are different among these intensity groups. Note that relatively large positive (negative) helicity being below (above) the boundary layer top is common in the baroclinic midlatitude atmosphere (Koprov et al., 2005).

The maximum helicity is located at ~100 m height inside the RMW in all groups. This height is close to the height of maximum inflow at the eyewall region. The helicity maximum is a result of in-up-and-out circulation (Levina and Montgomery, 2014), which may explain why the helicity maxima overlays the region of large radial gradient of inflow (Fig. 5). Negative helicity with a small magnitude is generally located outside of the RMW and above the boundary layer in all composites. Negative helicity that appears in the inner core region of TS and Cat12 groups may be a result of cyclonic subsidence in the eye (Gray and Shea, 1973).

The boundary layer height estimated based on the helicity method is close to each other in all three intensity groups, which increases with radius from ~300 m near the storm center to ~900 m at r* = 6. This height scale is smaller than the inflow layer depth in all intensity groups, and the difference between these two height scales decreases with storm intensity (Fig. 5). This result is consistent with that based on averaged h_{infl} and h_H from individual dropsondes (c.f., Fig. 3). The normalized helicity-based boundary layer height is close to h_{vmax} in all intensity groups (Fig. 6). At a given radius, h_{vmax} and h_H slowly decreases with the storm intensity. Again, this result agrees with that based on the averaged h_{vmax} from individual dropsondes. The results of h_{vmax} and h_{infl} also confirm those of Z11 and Ren et al. (2020).

The storm-motion-relative 0–1 km layer integrated helicity (SMH) is shown in Fig. 7. The data has been rotated relative to the storm motion direction denoted by the black arrow. For all samples, large values of helicity ($> 500\ m^2s^{-2}$) are concentrated in the inner core region ($0.5 < r^* < 2$) and a maximum of $700\ m^2s^{-2}$ in the front side of the storm. The front-back asymmetry of helicity there is more pronounced in the TS and Cat12 groups, while it is nearly evenly distributed in azimuth in the Cat345 group. Very small values of helicity are observed close to the storm center. The magnitude of helicity in the RMW region is larger in more intense TCs. Note that helicity values in TCs are much higher than observations in mid-latitude supercell environments (Molinari and Vollaro, 2008). The front-back asymmetry of helicity was also shown in Bogner et al. (2000). The horizontal view of storm-relative 0–1 km layer integrated helicity normalized by the maximum value of the lowest 1 km is shown in Fig. 8. Overall, the normalized helicity is more symmetrically distributed than the non-normalized helicity for All, TS and Cat12 groups. Again, the helicity magnitude increases with storm intensity. The front-right quadrant has the largest normalized helicity in all three groups in the inner core region ($r^* < 3$).

The shear-relative 0–1 km layer integrated helicity is shown in Fig. 9. The green arrow is the shear direction. The helicity in the downshear side is larger than that in the upshear side in ALL with a maximum in the downshear-left quadrant. This asymmetric structure is similar as in Hurricane Bonnie documented by (Molinari and Vollaro, 2008; Molinari, 2010). Relatively large downshear-upshear asymmetry appears in the TS and Cat12 groups, while the degree of asymmetry is

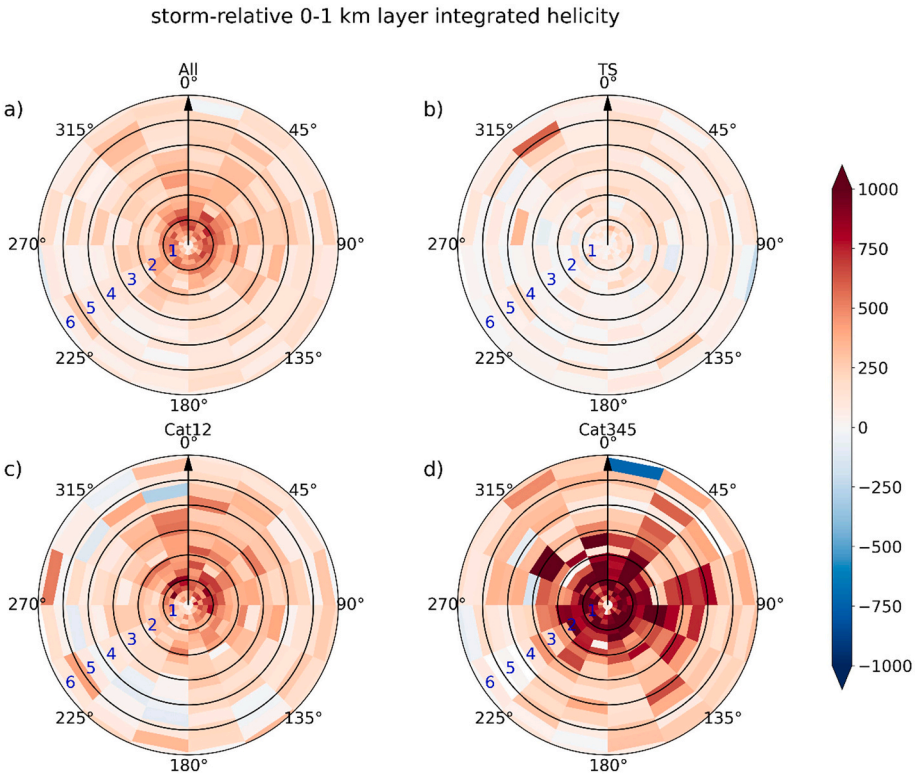

Fig. 7. Horizontal distribution of surface to 1 km integrated helicity in the storm-relative framework for a) All data, b) tropical-storm group, c) category 1–2 hurricane group, and d) category 3–5 hurricane group. The black arrow in each panel depicts the storm motion direction.

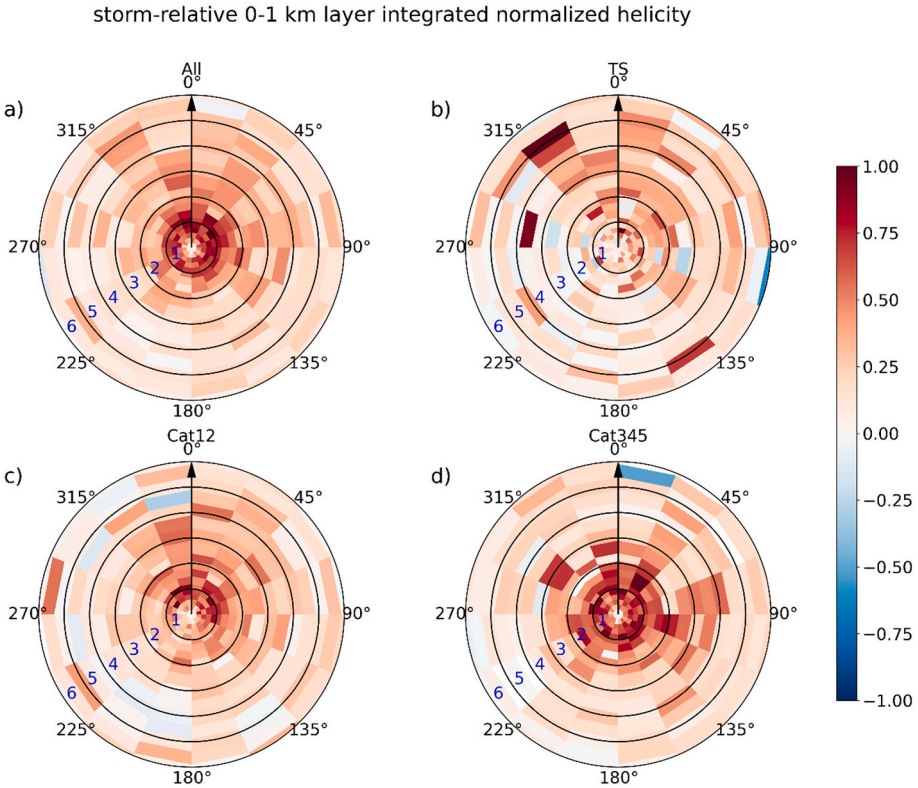

Fig. 8. Horizontal distribution of surface to 1 km integrated helicity normalized by the maximum value in the storm-relative framework for a) All data, b) tropical-storm group, c) category 1–2 hurricane group, and d) category 3–5 hurricane group. The black arrow in each panel depicts the storm motion direction.

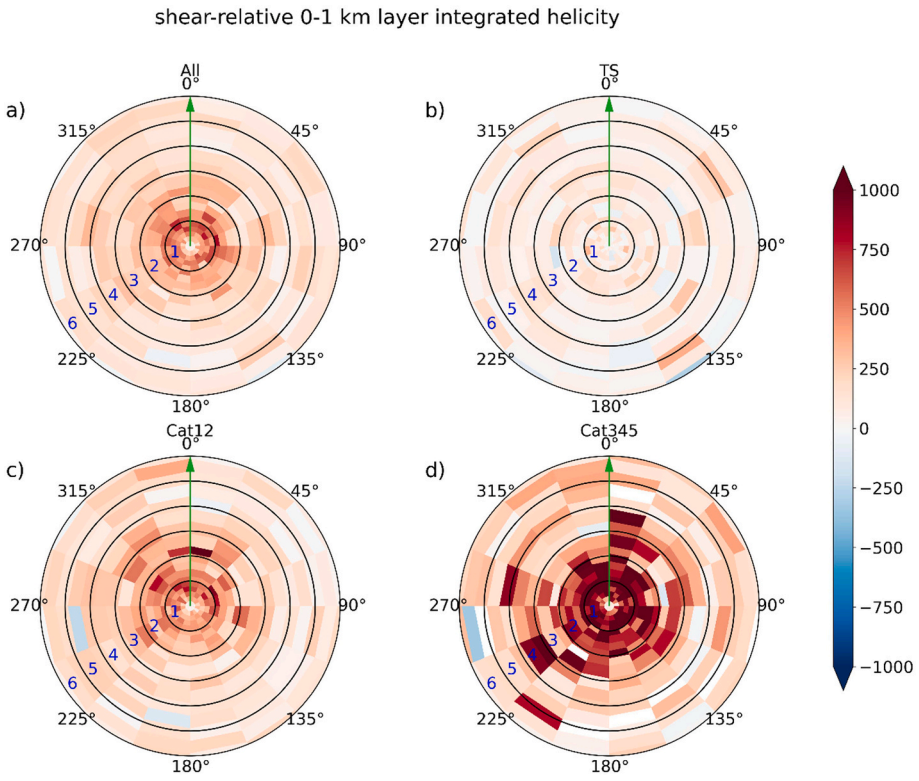

Fig. 9. Horizontal distribution of surface to 1 km integrated helicity in the shear-relative framework for a) All data, b) tropical-storm group, c) category 1–2 hurricane group, and d) category 3–5 hurricane group. The green arrow in each panel depicts the shear direction. (For interpretation of the references to color in this figure legend, the reader is referred to the web version of this article.)

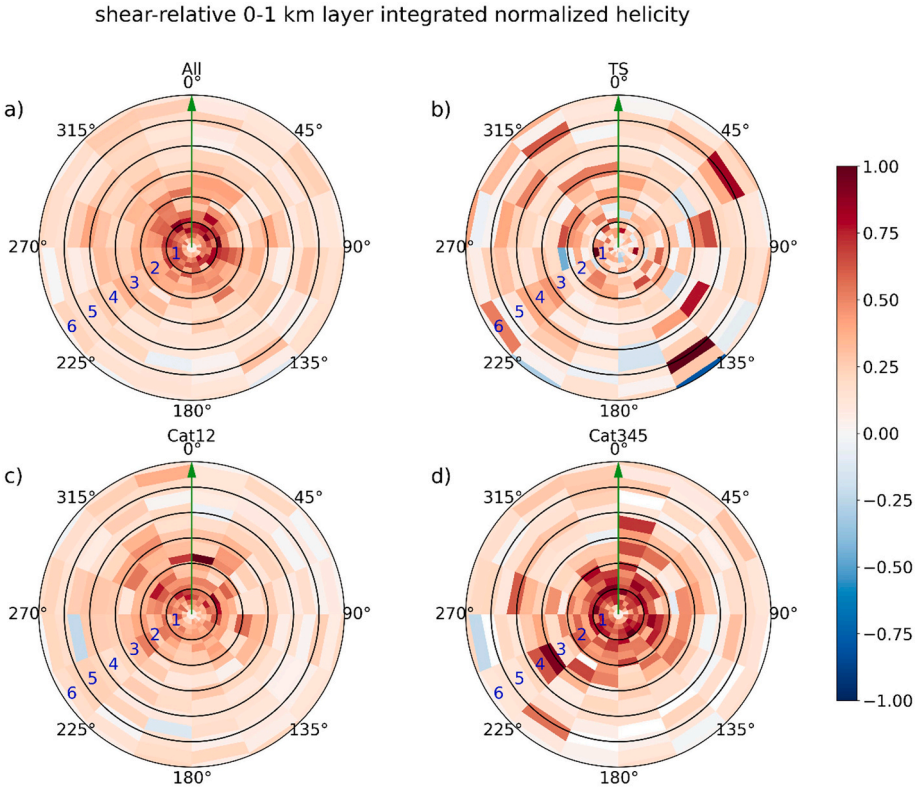

Fig. 10. Horizontal distribution of surface to 1 km integrated helicity normalized by the maximum value in the shear-relative framework for a) All data, b) tropical-storm group, c) category 1–2 hurricane group, and d) category 3–5 hurricane group. The green arrow in each panel depicts the shear direction.

small in the Cat345 group in the eyewall region. The helicity downshear is larger than upshear in the region right outside the eyewall ($1.5 < r^* < 2$) in the Cat345 group. There is a left-of-shear and right-of-shear asymmetry for $r^* > 3$ and the helicity left of shear is larger. The helicity magnitude is larger in more intense TCs, especially in regions inside $r^* < 5$. The downshear to upshear asymmetry in the inner core regions ($r^* < 3$) is also observed for the normalized helicity (Fig. 10). The degree of asymmetry is largest in the Cat12 group. Again,

the magnitude of the normalized helicity at $0.5 < r^* < 1.5$ increases with storm intensity.

5. Discussion and conclusion

In this study, more than 10 thousand GPS dropsonde profiles collected in Atlantic hurricanes from 1997 to 2017 were analyzed to investigate the three-dimensional structure of the TCBL with focus on the behavior of the boundary layer height and helicity distribution. We estimated the boundary layer height using helicity and compared this height scale to those studied in previous literature. Our results confirmed the radial variations of the inflow layer depth and jet height in dropsonde composites presented in previous studies. Our result showed that the helicity-based boundary layer height is close to the height of maximum tangential wind speed (i.e., the jet), which is located between the inflow layer depth and thermodynamic mixed layer height in all intensity groups. The kinematic boundary layer heights including the helicity method generally decrease with storm intensity at each radius. The three kinematic height scales tend to converge in major hurricanes, while the inflow layer is much deeper than the other two in the TS group.

Composites of normalized helicity show positive helicity in the boundary layer and negative helicity above the boundary layer but with a smaller magnitude in all intensity groups. The maximum normalized helicity is located at 100–200 m altitude and increases with radius in all intensity categories. This height is close to that of the maximum inflow. The maximum helicity is close to the maximum radial gradient of inflow that is located inward from the RMW. Positive helicity values near the RMW are much larger than those in the outer region.

Above the boundary layer, the normalized helicity is mainly negative. The layer-averaged non-normalized and normalized helicity show front and back asymmetry at the region close to the RMW in all three intensity groups. The helicity in the front is larger than that in the back of the storm and the degree of this asymmetry is larger in the TS and Cat12 groups than in the Cat345 group. There is also a downshear and upshear asymmetry close to the RMW in all intensity groups. The downshear helicity is larger than upshear. Furthermore, the left-shear helicity is larger than right-shear in the outer core region ($r^* > 3$). The magnitude of both normalized and non-normalized helicity is larger in stronger storms.

Negative helicity above the boundary layer indicates the dissipation of turbulent eddies (Frisch, 1995). The helicity being positive in the boundary layer and negative above has also been observed in a frontogenesis case (Tan and Wu, 1994). Deusebio and Lindborg (2014) found that the injection of negative helicity is caused by super-geostrophic wind in the uppermost part of the Ekman layer. The sign and magnitude differences in helicity between TC and non-TC cases may be due to differences in stability and degree of baroclinity. Negative helicity near the surface in the TC outer region is likely induced by surface friction.

Frisch (1995) showed that the rate of change of helicity is caused by kinematic viscosity and mean vortical helicity. Thus, subsidence in the TC eye contributes to the negative helicity near the storm center. Despite the absence of vertical velocity in the helicity calculation using dropsonde data, negative values of helicity are seen in the inner core region. A thin outflow layer above the boundary layer may be the reason for the negative helicity there. We note that the components of helicity related to horizontal velocity gradients cannot be determined using single dropsonde profiles. These terms may be large in eyewall and rainband regions. Future studies will quantify these terms using numerical simulations of TCs. Observations of these helicity components using other types of observations in the TCBL will also be explored in future work.

Helicity represents characteristics of turbulence in the boundary layer (Moffatt, 1983; Chkhetiani, 2001). Because of the similarity of the pressure and transport terms in TKE and helicity budgets (Zhang, 2010; Deusebio and Lindborg, 2014), helicity has the potential to be used to illustrate the TKE distribution in TCs. Deusebio and Lindborg (2014) found that the kinetic energy spectrum and helicity spectrum in the boundary layer have a good correlation and can be fitted to $k^{-5/3}$ power law at high frequencies. In a moderate rotating system, energy transportation between different scales is found to be related to helicity (Mininni and Pouquet, 2009). Our dropsonde based distribution of helicity in the TCBL is similar to those based on Doppler radar observed TKE by Lorsolo et al. (2010), suggesting the linkage of helicity and turbulence strength. The close resemblance between TKE and helicity distributions suggests that the helicity method for boundary layer height may be applied in TKE-type boundary layer schemes. Turbulent energy cascade by turbulent eddies with different scales has been studied using aircraft observations (Byrne and Zhang, 2013) and tower observations (Tang et al., 2015) in the TCBL. Our result shows that the maximum helicity is located where the inverse energy cascade may occur (i.e., ~150 m altitude) in TCs. It is worthwhile to explore how helicity is linked energy cascade process in future studies.

Author statement

Nuo Chen: Data curation; Formal analysis; Methodology and Software; **Jie Tang**: Conceptualization and Project administration; Writing - original draft and Funding acquisition; **Jun A. Zhang**: Supervision; Writing - review & editing. **Lei-Ming Ma**: Validation; Supervision. **Hui Yu**: Supervision.

Declaration of Competing Interest

We,all of the authors, declared that we have no commercial and personal relationships with other people or organizations that can inappropriately influence our work, there is no professional or other personal interest of any nature or kind in any product, service and/or company that could be construed as influencing the position presented in, or the review of, the manuscript entitled.

Acknowledgement

Jie Tang and Nuo Chen are supported by the Key Program for International S&T Cooperation Projects of China (No. 2017YFE0107700), Key special projects of the Ministry of Science and Technology (2018YFC1506403) and the National Natural Science Foundation of China (No. 41475060 and 41775065). Jun Zhang was supported by NOAA grant NA14NWS4680030, NSF Grant AGS1822128 and ONR grant N00014-20-1-2071.

References

Ahern, K., Bourassa, M.A., Hart, R.E., Zhang, J.A., Rogers, R.F., 2019. Observed kinematic and thermodynamic structure in the hurricane boundary layer during intensity change. Mon. Weather Rev. 147, 2765–2785.

Barnes, G.M., 2008. Atypical thermodynamic profiles in hurricanes. Mon. Weather Rev. 136, 631–643.

Bell, M.M., Montgomery, M.T., 2008. Observed Structure, Evolution, and Potential Intensity of Category 5 Hurricane Isabel (2003) from 12 to 14 September. 136. pp. 2023–2046.

Bogner, P.B., Barnes, G.M., Franklin, J.L., 2000. Conditional instability and shear for six hurricanes over the Atlantic Ocean. Wea. Forecasting 15, 192–207.

Braun, S.A., Tao, W.K., 2000. Sensitivity of high-resolution simulations of Hurricane Bob (1991) to planetary boundary layer parameterizations. Mon. Weather Rev. 128, 3941–3961.

Brown, R.A., 1970. A Secondary Flow Model for the Planetary Boundary Layer. 27. pp. 742–757.

Bu, Y.P., Fovell, R.G., Corbosiero, K.L., 2017. The influences of boundary layer vertical mixing and cloud-radiative forcing on tropical cyclone size. J. Atmos. Sci. 74, 1273–1292.

Byrne, D., Zhang, J.A., 2013. Height-dependent transition from 3-D to 2-D turbulence in the hurricane boundary layer. Geophys. Res. Lett. 40 (7), 1439–1442. https://doi.org/10.1002/grl.50335.

Chen, X., Zhang, J.A., Marks, F.D., 2019. A thermodynamic pathway leading to rapid intensification of tropical cyclones in shear. Geophys. Res. Lett. 46 (15), 9241–9251.

Chkhetiani, O.G., 2001. On the helical structure os the Ekman boundary layer. Izvestiya. Atmosph. Oceanic Phys. 37, 8.
Cione, J.J., Coauthors, 2020. Eye of the storm: observing hurricanes with a small unmanned aircraft system. Bull. Am. Meteorol. Soc. 101, E186–E205.
Davies-Jones, R., 1984. Streamwise Vorticity: The Origin of Updraft Rotation in Supercell Storms. 41. pp. 2991–3006.
Demuth, J., DeMaria, M., Knaff, J.A., 2006. Improvement of advanced microwave sounder unit tropical cyclone intensity and size estimation algorithms. J. Appl. Meteorol. 45, 1573–1581.
Deusebio, E., Lindborg, E., 2014. Helicity in the Ekman boundary layer. J. Fluid Mech. 755, 654–671.
Emanuel, K.A., 1986. An Air-Sea Interaction Theory for Tropical Cyclones. Part I: Steady-State Maintenance. 43. pp. 585–605.
Etling, D.J.B., 1985. Some Aspects of Helicity in Atmospheric Flows. 58. pp. 88–100.
Fetzer, E.J., Teixeira, J., Olsen, E.T., Fishbein, E.F., 2004. Satellite Remote Sounding of Atmospheric Boundary Layer Temperature Inversions Over the Subtropical Eastern Pacific. 31.
Foster, R.C., 2009. Boundary-layer similarity under an axisymmetric, gradient wind vortex. Bound.-Layer Meteorol. 131, 321–344.
Frisch, U., 1995. Turbulence, the Legacy of A.N. Kolmogorov. Cambridge University Press.
Gray, W.M., Shea, D.J., 1973. The Hurricane's inner core region. II. Thermal stability and dynamic characteristics. J. Atmos. Sci. 30, 1565–1576.
Guimond, S.R., Zhang, J.A., Sapp, J.W., Frasier, S.J., 2018. Coherent turbulence in the boundary layer of Hurricane Rita (2005) during an eyewall replacement cycle. J. Atmos. Sci. 75, 3071–3093.
Hide, R., 1989. Superhelicity, helicity and potential vorticity. Geophys. Astrophys. Fluid Dynam. 48, 69–79.
Hock, T.F., Franklin, J.L., 1999. The NCAR GPS dropwindsonde. Bull. Amer. Meteor. Soc. 80, 407–420.
Kepert, J.D., 2006a. Observed boundary layer wind structure and balance in the hurricane core. Part I: hurricane Georges. J. Atmos. Sci. 63, 2169–2193.
Kepert, J.D., 2006b. Observed boundary layer wind structure and balance in the hurricane core. Part I: hurricane Georges. J. Atmos. Sci. 63, 2169–2193.
Kepert, J.D., 2012. Choosing a boundary layer parameterization for tropical cyclone modeling. Mon. Weather Rev. 140, 1427–1445.
Kieu, C.Q., Tallapragada, V., Hogsett, W., 2014. On the onset of the tropical cyclone rapid intensification in the HWRF model. Geophys. Res. Lett. 9, 3298–3306.
Koprov, B.M., Koprov, V.M., Ponomarev, V.M., Chkhetiani, O.G., 2005. Experimental studies of turbulent helicity and its spectrum in the atmospheric boundary layer. Dokl. Phys. 50, 419–422.
Krainchnan, R.H., 1967. Inertial ranges in two-dimensional turbulence. Phys. Fluids 10, 1417.
Krause, F., Rädler, K.-H., 1980. Mean-Field Magnetohydrodynamics and Dynamo Theory. Akademie, Berlin and Pergamon Press, Oxford.
Levina, G.V., Montgomery, M.T., 2014. Tropical cyclogenesis: a numerical diagnosis based on helical flow organization. J. Phys. Conf. Ser. 544. https://doi.org/10.1088/1742-6596/544/1/012013.
Levy, Y., Degani, D., Seginer, A., 1990. Graphical visualization of vortical flows by means of helicity. AIAA J. 28, 1347–1352.
Lorsolo, S., Zhang, J.A., Marks, F., Gamache, J., 2010. Estimation and mapping of hurricane turbulent energy using airborne Doppler measurements. Mon. Weather Rev. 138, 3656–3670.
Ma, L.M., Bao, X.W., 2016. Parametrization of planetary boundary-layer height with helicity and verification with tropical cyclone prediction. Bound.-Layer Meteorol. 160, 569–593.
Markowski, P.M., Richardson, Y., 2010. Organization of isolated convection. Mesoscale Meteorol. Midlat. 201–244.
Marks, F.D., Black, P.G., Montgomery, M.T., Burpee, R.W., 2008. Structure of the eye and eyewall of Hurricane Hugo (1989). Mon. Weather Rev. 136, 1237–1259.
Medeiros, B., Hall, A., Stevens, B., 2005. What controls the mean depth of the PBL? J. Clim. 18, 3157–3172.
Ming, J., Zhang, J.A., 2016. Effects of surface flux parameterization on numerically simulated intensity and structure of Typhoon Morakot (2009). Adv. Atmos. Sci. 33, 58–72.
Ming, J., Zhang, J.A., Rogers, R.F., 2015. Typhoon kinematic and thermodynamic boundary layer structure from dropsonde composites. J. Geophs. Res. Atoms. 120, 3158–3172.
Mininni, P.D., Pouquet, A., 2009. Helicity cascades in rotating turbulence. Phys. Rev. E Stat. Nonlinear Soft Matter Phys. 79, 026304.
Moffat, H.K., Tsinober, A., 1992. Helicity in laminar and turbulent flow. Annu. Rev. Fluid Mech. 32.
Moffatt, H.K., 1983. Magnetic Field Generation in Electrically Conducting Fluids. Cambridge University Press.
Molinari, J., Vollaro, D., 2010. Distribution of helicity, CAPE, and shear in tropical cyclones. J. Atmos. Sci. 67, 274–284.
Molinari, J., Vollaro, D., 2008. Extreme helicity and intense convective towers in hurricane bonnie. Mon. Weather Rev. 136, 4355–4372.
Molinari, J., Frank, J., Vollaro, D., 2013. Convective bursts, downdraft cooling, and boundary layer recovery in a sheared tropical storm. Mon. Weather Rev. 141, 1048–1060.
Montgomery, M.T., Smith, R.K., 2014. Paradigms for tropical cyclone intensification. Aust. Meteor. Oceanogr. J. 64, 37–66.
Montgomery, M.T., Zhang, J.A., Smith, R.K., 2014. An analysis of the observed low-level structure of rapidly intensifying and mature hurricane Earl (2010). Quart. J. Roy. Meteor. Soc. 140, 2132–2146.
Nguyen, L.T., Rogers, R., Zawislak, J., Zhang, J.A., 2019. Assessing the influence of convective downdrafts and surface enthalpy fluxes on tropical cyclone intensity change in moderate vertical wind shear. Mon. Weather Rev. 147, 3519–3534.
Nolan, D.S., Stern, D.P., Zhang, J.A., 2009. Evaluation of planetary boundary layer parameterizations in tropical cyclones by comparison of in situ observations and high-resolution simulations of hurricane Isabel (2003). Part II: inner-core boundary layer and eyewall structure. Mon. Weather Rev. 137, 3675–3698.
Nolan, D.S., Zhang, J.A., Stern, D.P., 2009a. Evaluation of planetary boundary layer parameterizations in tropical cyclones by comparison of in situ observations and high-resolution simulations of hurricane Isabel (2003). Part I: initialization, maximum winds, and the outer-core boundary layer. Mon. Weather Rev. 137, 3651–3674.
Onderlinde, M.J., Nolan, D.S., 2014. Environmental helicity and its effects on development and intensification of tropical cyclones. J. Atmos. Sci. 71, 4308–4320.
Pichler, H., Schaffhauser, A., 1998. The synoptic meaning of helicity. Meteorog. Atmos. Phys. 66, 23–34.
Ren, Y., Zhang, J.A., Guimond, S.R., Wang, X., 2019. Hurricane boundary layer height relative to storm motion from GPS dropsonde composites. Atmosphere 10, 1.
Ren, Y., Zhang, J.A., Vigh, J.L., Zhu, P., Liu, H., Wang, X., Wadler, J.B., 2020. An observational study of the symmetric boundary layer structure and tropical cyclone intensity. Atmosphere 11, 158.
Riemer, M., Montgomery, M.T., Nicholls, M.E., 2010. A new paradigm for intensity modification of tropical cyclones: thermodynamic impact of vertical wind shear on the inflow layer. Atmos. Chem. Phys. 10, 3163–3188.
Rogers, R.F., Reasor, P.D., Zhang, J.A., 2015. Multiscale structure and evolution of hurricane Earl (2010) during rapid intensification. Mon. Weather Rev. 143, 536–562.
Rogers, R.F., Zhang, J.A., Zawislak, J., Jiang, H., III, G.R.A., Zipser, E.J., Stevenson, S.N., 2016. Observations of the structure and evolution of hurricane Edouard (2014) during intensity change. Part II: kinematic structure and the distribution of deep convection. Mon. Weather Rev. 144, 3355–3376.
Simmons, A. and Coauthors, 2020: Global Stratospheric Temperature Bias and Other Stratospheric Aspects of ERA5 and ERA5.1. ECMWF Technical Memoranda.
Smith, R.K., Montgomery, M.T., 2010. Hurricane boundary-layer theory. Quart. J. Roy. Meteor. Soc. 136, 1665–1670.
Smith, R.K., Thomsen, G.L., 2010. Dependence of tropical-cyclone intensification on the boundary-layer representation in a numerical model. Quart. J. Roy. Meteor. Soc. 136, 1671–1685.
Smith, R.K., Montgomery, M.T., Van Sang, N., 2009. Tropical cyclone spin-up revisited. Quart. J. Roy. Meteor. Soc. 135, 1321–1335.
Smith, R.K., Zhang, J.A., Montgomery, M.T., 2017. The dynamics of intensification in a hurricane weather research and forecasting simulation of Hurricane Earl (2010). Quart. J. Roy. Meteor. Soc. 143, 293–308.
Stull, R.B., 1988. An Introduction to Boundary Layer Meteorology. (Springer Netherlands).
Tallaprgada, V., Kieu, C., Kwon, Y., Trahan, S., Liu, Q., Zhang, Z., Kwon, I., 2014. Evaluation of storm structure from the operational HWRF model during 2012 implementation. Mon. Weather Rev. 142, 4308–4325.
Tan, Zhemin, Wu, Rongsheng, 1994. Helicity dynamics of atmospheric flow. Adv. Atmos. Sci. 11, 175–188.
Tang, J., Byrne, D., Zhang, J.A., Wang, Y., Lei, X., Wu, D., Fang, P., Zhao, B., 2015. Horizontal transition of turbulent cascade in the near-surface layer of tropical cyclones. J. Atmos. Sci. 72, 4915–4925.
Tang, J., Zhang, J.A., Kieu, C., Marks, F.D., 2018. Sensitivity of hurricane intensity and structure to two types of planetary boundary layer parameterization schemes in idealized HWRF simulations. Trop. Cycl. Res. Rev. 7, 201–211.
Wadler, J.B., Zhang, J.A., Jaimes, B., Shay, L.K., 2018. Downdrafts and the evolution of boundary layer thermodynamics in hurricane Earl (2010) before and during rapid intensification. Mon. Weather Rev. 146, 3545–3565.
Wang, Y., 2012. Recent research progress on tropical cyclone structure and intensity. Trop. Cyclone Res. Rev. 1, 254–275.
Wang, Y., Wu, C.-C., 2004. Current understanding of tropical cyclone structure and intensity changes-a review. Meteorog. Atmos. Phys. 87, 257–278.
Weisman, M.L., Rotunno, R., 2000. The Use of Vertical Wind Shear versus Helicity in Interpreting Supercell Dynamics. 57. pp. 1452–1472.
Willoughby, H.E., Chelmow, M., 1982. Objective determination of hurricane tracks from aircraft observations. Mon. Weather Rev. 110, 1298–1305.
Zawislak, J.H., Jiang III, G.R.A., Zipser, E.J., Rogers, R.F., Zhang, J.A., Stevenson, S.N., 2016. Observations of the structure and evolution of hurricane Edouard (2014) during intensity change. Part I: relationship between the thermodynamic structure and precipitation. Mon. Weather Rev. 144, 3333–3354.
Zeng, X., M. A. Brunke, M. Zhou, C. Fairall, N. A. Bond, D. H. Lenschow, 2004. Marine Atmospheric Boundary Layer Height over the Eastern Pacific: Data Analysis and Model Evaluation. J. Clim. 17, 4159–4170. https://doi.org/10.1175/JCLI3190.1.
Zhang, J.A., 2010. Estimation of dissipative heating using low-level in-situ aircraft observations in the hurricane boundary layer. J. Atmos. Sci. 67, 1853–1862.
Zhang, J.A., Marks, F.D, Sippel, J.A., Rogers, R.F., Zhang, S.G., Gopalakrishnan, S.G., Zhang, Z., Tallapragada, V., 2018. Evaluating the Impact of Improvement in the Horizontal Diffusion Parameterization on Hurricane Prediction in the Operational Hurricane Weather Research and Forecast (HWRF) Model. 33. pp. 317–329. https://doi.org/10.1175/WAF-D-17-0097.1.
Zhang, J.A., Drennan, W.M., 2012. An observational study of vertical eddy diffusivity in the hurricane boundary layer. J. Atmos. Sci. 69, 3223–3236.
Zhang, J.A., Marks, F.D., 2015. Effects of horizontal eddy diffusivity on tropical cyclone intensity change and structure in idealized three-dimensional numerical simulations. Mon. Weather Rev. 2015 (143), 3981–3995.
Zhang, J.A., Rogers, R.R., 2019. Effects of parameterized boundary layer structure on

hurricane rapid intensification in shear. Mon. Weather Rev. 2019 (147), 853–871.
Zhang, J.A., Rogers, R.F., Nolan, D.S., Marks, F.D., 2011a. On the characteristic height scales of the hurricane boundary layer. Mon. Weather Rev. 139, 2523–2535.
Zhang, J.A., Marks, F.D., Montgomery, M.T., Lorsolo, S., 2011b. An estimation of turbulent characteristics in the low-level region of intense Hurricanes Allen (1980) and Hugo (1989). Mon. Weather Rev. 139, 1447–1462.
Zhang, J.A., Rogers, R.F., Reasor, P.D., Uhlhorn, E.W., Marks, F.D., 2013. Asymmetric hurricane boundary layer structure from dropsonde composites in relation to the environmental vertical wind shear. Mon. Weather Rev. 141, 3968–3984.
Zhang, J.A., Nolan, D.S., Rogers, R.F., Tallapragada, V., 2015. Evaluating the Impact of Improvements in the Boundary Layer Parameterization on Hurricane Intensity and Structure Forecasts in HWRF. 143. pp. 3136–3155.
Zhang, J.A., Rogers, R.F., Tallapragada, V., 2017a. Impact of parameterized boundary layer structure on tropical cyclone rapid intensification forecasts in HWRF. Mon. Weather Rev. 145, 1413–1426.
Zhang, J.A., Cione, J.J., Kalina, E.A., Uhlhorn, E.W., Hock, T., Smith, J.A., 2017b. Observations of Infrared Sea Surface Temperature and Air–Sea Interaction in Hurricane Edouard (2014) using GPS Dropsondes. 34. pp. 1333–1349.
Zhang, J.A., Dunion, J.P., Nolan, D.S., 2020. In situ observations of the diurnal variation in the boundary layer of mature hurricanes. Geophys. Res. Lett. 7 (3). https://doi.org/10.1029/2019GL086206.
Zhao, Z., Chan, P.W., Wu, N., Zhang, J.A., Hon, K.K., 2020. Aircraft observations of turbulent characteristics in the tropical cyclone boundary layer. Bound.-Layer Meteorol. 174 (3), 493–511.
Zhu, P., Menelaou, K., Zhu, Z., 2013. Impact of subgrid-scale vertical turbulent mixing on eyewall asymmetric structures and mesovortices of hurricanes. Quart. J. Roy. Meteor. Soc. 2013 (140), 416–438.
Zhu, P., Tyner, B., Zhang, J.A., Aligo, E., Gopalakrishnan, S., Marks, F.D., Mehra, A., Tallapragada, V., 2019. Role of eyewall and rainband eddy forcing in tropical cyclone intensification. Atmos. Chem. Phys. 19, 14,289–14,310.